How to cite: *Angew. Chem. Int. Ed.* **2025**, *64*, e202421790
doi.org/10.1002/anie.202421790

Nanozymes Hot Paper

t_2 Occupancy as an Effective and Predictive Descriptor for the Design of High-Performance Spinel Oxide Peroxidase-like Nanozymes

*Jiang Du[+], Zhenzhen Wang[+], Quan Wang[+], Xiang Gu, Xingfa Gao, and Hui Wei**

Abstract: Nanozymes are next generation of enzyme mimics. Due to the lack of activity descriptors, most nanozymes were discovered through trial-and-error strategies or by accident. While e_g occupancy in an octahedral crystal field was proven as an effective descriptor, the t_2 in a tetrahedral crystal field has rarely been explored. Here, we first identified t_2 occupancy as an effective and predictive descriptor. Then, we predicted and demonstrated that spinel oxide nanozymes (AB_2O_4) with a t_2 occupancy of around 4.4 at A site had the highest activity. Furthermore, we introduced O_β content as a secondary descriptor. The dual descriptor strategy resulted in a three-dimensional volcanic curve, converging at a vertex. To surpass the limitations of volcanic curves, a dual site optimizing strategy was proposed, guiding the optimization of both A and B sites as Cu and Co, respectively. The designed $CuCo_2O_4$ exhibited the highest activity, achieving around 100- and 2-fold enhancement compared to initial material and the state-of-the-art spinel oxide nanozyme $LiCo_2O_4$, respectively. Density functional theory calculations provided a theoretical basis for the catalytic process. This work provides a new strategy for the rational design of nanozymes, and t_2 occupancy may also be applicable to the design of other catalysts.

[*] J. Du,[+] Q. Wang,[+] X. Gu, H. Wei
College of Engineering and Applied Sciences, Nanjing National Laboratory of Microstructures, Jiangsu Key Laboratory of Artificial Functional Materials, Nanjing University, Nanjing, Jiangsu 210023, China
E-mail: weihui@nju.edu.cn

Z. Wang,[+] X. Gao
Laboratory of Theoretical and Computational Nanoscience, National Center for Nanoscience and Technology of China, Beijing 100190, China

H. Wei
State Key Laboratory of Analytical Chemistry for Life Science, School of Chemistry and Chemical Engineering, Chemistry and Biomedicine Innovation Center (ChemBIC), ChemBioMed Interdisciplinary Research Center at Nanjing University, Nanjing University, Nanjing, Jiangsu 210023, China

H. Wei
NMPA Key Laboratory for Biomedical Optics, Hangzhou, Zhejiang 310018, China

[+] These authors contributed equally to this work.

Introduction

Nanozymes are functional nanomaterials with enzyme-like catalytic activities.[1] Compared with their natural counterparts and conventional enzyme mimics, they possess superior characteristics such as low cost, high stability, and tunable structure and function, showing strong application capability and promising prospects in fields such as biosensing, disease diagnosis and therapy, environmental monitoring and protection, agriculture, and chemical synthesis.[2] Since the discovery of ferromagnetic nanoparticles with intrinsic peroxidase (POD) activity,[3] thousands of nanomaterials have been found to possess enzyme-like activities, including metals, alloys, metal oxides, carbon, and metal–organic frameworks.[4] However, most of them were discovered through trial-and-error strategy or by accident, which is mainly due to the lack of predictive descriptors.[5]

Sabatier's rule is a powerful principle to guide the design of catalysts.[6] Many descriptors based on it have been developed, such as d-band center, O 2p-band center, number of d-band electrons, oxidized state, and e_g occupancy.[7] Particularly, e_g occupancy has been demonstrated as an experimentally effective descriptor for the rational design of nanozymes.[5a,b] However, its applicability has only been demonstrated for the octahedral crystal field. t_2 represents the triple antibonding molecular orbitals (σ^*_{xy}, σ^*_{xz}, and σ^*_{yz}), generated by the splitting of d-orbital in the tetrahedral crystal field. It is similar with the antibonding occupied component of e_g in the octahedral crystal field.[7f] In addition, the tetrahedral site is the significant source of activity of spinel catalysts.[8] Nevertheless, to our knowledge, using t_2 occupancy as a direct descriptor in various fields and systematic studies on tetrahedral site have been rarely reported.

In this work, we first reported t_2 occupancy as an effective and predictive descriptor to guide the design of nanozymes. We chose spinel oxides (AB_2O_4, A and B occupy one tetrahedral center and two octahedral centers, respectively) as the model materials for POD-like activity, for possessing both tetrahedral and octahedral sites with easily tunable structures and enzyme-like activities,[9] and being widely applied in environmental detection,[10] bioassay,[11] antibacterial,[12] and anti-tumor treatment[13] as POD mimics, but their low POD-like activity limited the applications. We selected Cr, which can stably occupy octahedral site, as the B site element to systematically regulate the transition metal elements of A site as Mn, Fe, Co, Ni, Cu, and Zn, respectively.[9a,14] After investigating and calibrating the electronic arrangement, the accurate t_2

occupancies of A site in the as-prepared Cr-series spinel oxides were obtained. Encouragingly, t_2 occupancy exhibited a volcanic-like curve with specific activity, demonstrating that t_2 occupancy is an effective descriptor. $CuCr_2O_4$ with the highest specific activity was chosen as next model and we tuned the t_2 occupancy of Cu by changing the calcination temperatures of $CuCr_2O_4$ (400, 500, 600, 700, and 800 °C, respectively). Their specific activities and calibrated t_2 occupancies matched well with the volcanic curve. The specific activities reached the peak of the volcanic curve when t_2 occupancy was about 4.4, further demonstrating the effectiveness and predictive ability of t_2 occupancy as a descriptor. Subsequently, we proposed the surface oxygen (O_β) content as a secondary descriptor to interpret the different activities with similar t_2 occupancy, while t_2 occupancy remained as the primary activity descriptor. The dual descriptors strategy converged to a vertex, resulting in a three-dimensional volcanic curve. Combining with our previous work, the dual sites optimizing strategy was proposed where A and B sites were optimized as Cu and Co, respectively. The resulting material $CuCo_2O_4$ exhibited the best specific activity and broke through the limits of volcanic curve, obtaining around a hundredfold increase compared with the initial materials, an order of magnitude increase over most reported nanozymes, and a twofold increase relative to $LiCo_2O_4$ which was proved the best specific activity in previous work. Finally, the above conclusions were further validated and rationalized through density functional theory (DFT) calculations.

Results and Discussion

POD-Like Activities of Cr-Series Spinel Oxide Nanozymes

Spinel oxides can be classified into three types: normal, inverse, and complex, which are mainly distinguished by the degree of mutual substitution and occupation of metal elements at A and B sites.[9a] To minimize the impact of different crystal structures of spinels and to identify the determining factors in the activity of nanozymes, we chose six chromium-series spinel oxides (ACr_2O_4, A = Mn, Fe, Co, Ni, Cu, and Zn, in which Cr can occupy the octahedral site stably) to investigate the effect of AO_4 tetrahedral structure on POD-like activities (Figure 1a). $MnCr_2O_4$ and $NiCr_2O_4$ were synthesized with a coprecipitation method,[15] $FeCr_2O_4$ was synthesized with a solution combustion synthesis method,[16] and $CuCr_2O_4$ (calcination temperature was 800 °C) and $CoCr_2O_4$ were synthesized with a hydrothermal method.[17] Note, $ZnCr_2O_4$ has been investigated in our previous work,[5b] and here we quoted it directly for comparison (Table S4). The as-prepared spinel oxides were characterized by using transmission electron microscope (TEM), powder X-ray diffraction (PXRD), inductively coupled plasma atomic emission spectrometer (ICP-AES), X-ray photoelectron spectroscopy (XPS), Brunauer–Emmett–Teller (BET) surface area, and magnetic measurements (Figures S1, S4, and S5, and Tables S1 and S3). The TEM images (Figure 1d-h) revealed the uniform nanoscale particles and typical irregular morphology features of spinel oxides. The as-prepared samples inevitably differed in size

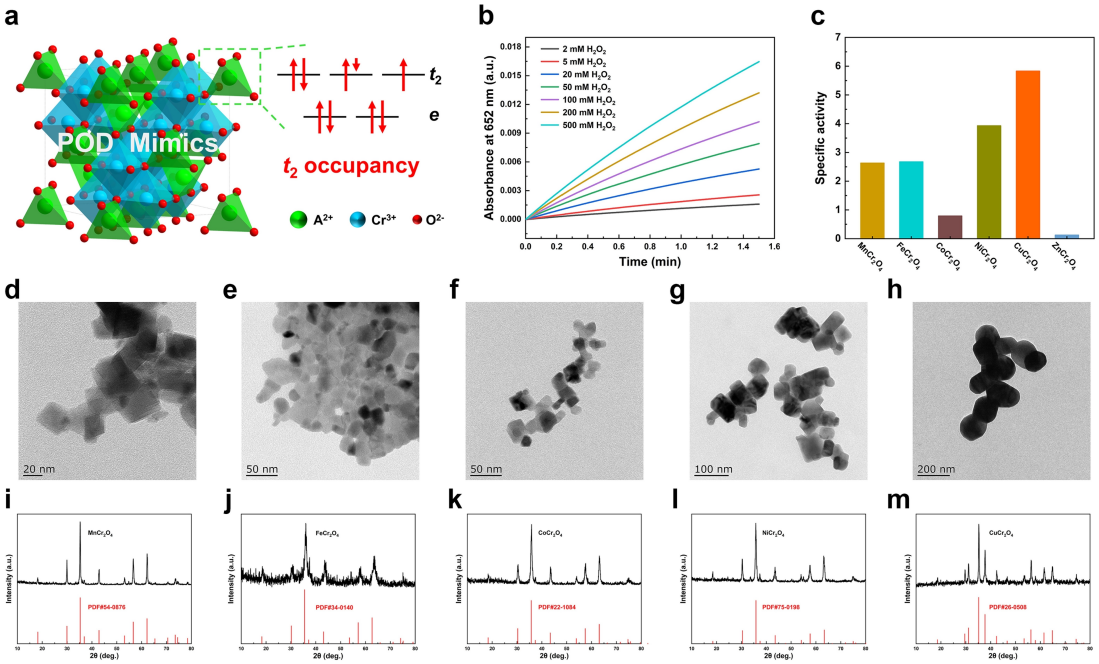

Figure 1. Cr-series spinel oxide nanozymes as POD mimics. (a) Scheme of investigating t_2 occupancy at tetrahedral site with AO_4 structure for POD-like activity. Cr, A, and O are displayed in blue, green, and red, respectively. (b) Time evolution of absorbance at 652 nm for monitoring the catalytic oxidation of 1 mM TMB with different concentrations of H_2O_2 in the presence of 20 μg/mL $CuCr_2O_4$. (c) Specific POD-like activities of ACr_2O_4 (A=Mn, Fe, Co, Ni, Cu, and Zn). (d-h) TEM images of ACr_2O_4 (A=Mn, Fe, Co, Ni, and Cu). (i–m) XRD patterns of ACr_2O_4 (A=Mn, Fe, Co, Ni, and Cu).

for the different ion sizes and electronic structures of constituent elements. The XRD patterns of each as-prepared sample (Figure 1i-m) displayed a set of peaks corresponding to their respective standard cards (red line, PDF#54–0876, PDF#34–0140, PDF#22–1084, PDF#75–0198, and PDF#26–0508, respectively) and matched well, indicating typical spinel structures. The Mn $2p_{1/2}$ peak at 653.5 eV and Mn $2p_{3/2}$ peak at 641.5 eV,[18] Fe $2p_{1/2}$ peak at 724.2 eV and Fe $2p_{3/2}$ peak at 710.9 eV,[19] Co $2p_{1/2}$ peak at 796.5 eV and Co $2p_{3/2}$ peak at 780.7 eV with two corresponding satellites at 802.7 eV and 786.2 eV,[20] Ni $2p_{1/2}$ peak at 873.3 eV and Ni $2p_{3/2}$ peak at 855.8 eV,[19a] and Cu $2p_{1/2}$ peak at 954.1 eV and Cu $2p_{3/2}$ peak at 934.6 eV with strong Cu^{2+} satellites[21] were correspond to A^{2+} (A = Mn, Fe, Co, Ni, and Cu). In addition, the peaks of around 586.3 eV and 576.3 eV represented the Cr^{3+} $2p_{1/2}$ and Cr^{3+} $2p_{3/2}$[22] though some slight peak shift were observed in different spinel oxides(Figure S1). The above results demonstrated the successful synthesis of all the spinel oxides.

3,3′,5,5′-tetramethylbenzidine (TMB) is a typical POD substrate, and its blue oxidized product of TMB (oxTMB) possesses a characteristic absorption peak at 652 nm. The intrinsic POD-like activities of Cr-series spinel oxides were determined by using absorption spectroscopy to monitor the catalytic oxidation process of TMB with hydrogen peroxide (H_2O_2) in the presence of the nanozymes (Figures 1b and S2). The V_{max} of Cr-series spinel oxide nanozymes was defined as mass activity, which was determined by conducting steady-state kinetic assays and calculated by drawing and fitting a double reciprocal plot through the Michaelis-Menten equation (Figure S3). The surface areas of Cr-series spinel oxide nanozymes were normalized based on the BET surface areas obtained by nitrogen adsorption-desorption measurements (Figure S4). The specific activities, obtained by using the corresponding normalized BET areas, were used to assess the POD-like activities of Cr-series spinel oxide nanozymes to exclude the differences in activity caused by variations in their surface areas and explore the intrinsic activity differences caused by t_2 occupancy (referring to the Experimental Section for details of above methods). As shown in Figure 1c, $CuCr_2O_4$ possessed the highest specific activity, indicating that Cu may be the highly active element of tetrahedron site. The pH-dependent behavior of $CuCr_2O_4$ was tested (Figure S6), indicating the significant activity in acidic environments. Particularly, it is encouraging to note that tetrahedral site is also a significant source of POD-like activity due to Cr being an inactive element in POD-like process of spinel nanozymes.[5b]

Evaluating the Effectiveness and Predictive Capacity of t_2 Occupancy as a Descriptor

Since the octahedral sites were fixed, the above control variable results revealed that the POD-like activities of spinel oxide nanozymes were indeed related to the transition metal cations in the tetrahedral field with AO_4 structure. The electron arrangements of A site transition metal cations of Cr-series spinel oxides were then investigated and calibrated (referring to the Experimental Section for details) to obtain the accurate electronic arrangements and t_2 occupancies of A site of the actual as-prepared Cr-series spinel materials (Figures 2a and S5, and Tables S2–S4).

After obtaining the accurate t_2 occupancy of A site, we plotted the specific activity of the as-prepared Cr-series spinel oxide nanozymes as the y-axis against the correspond-

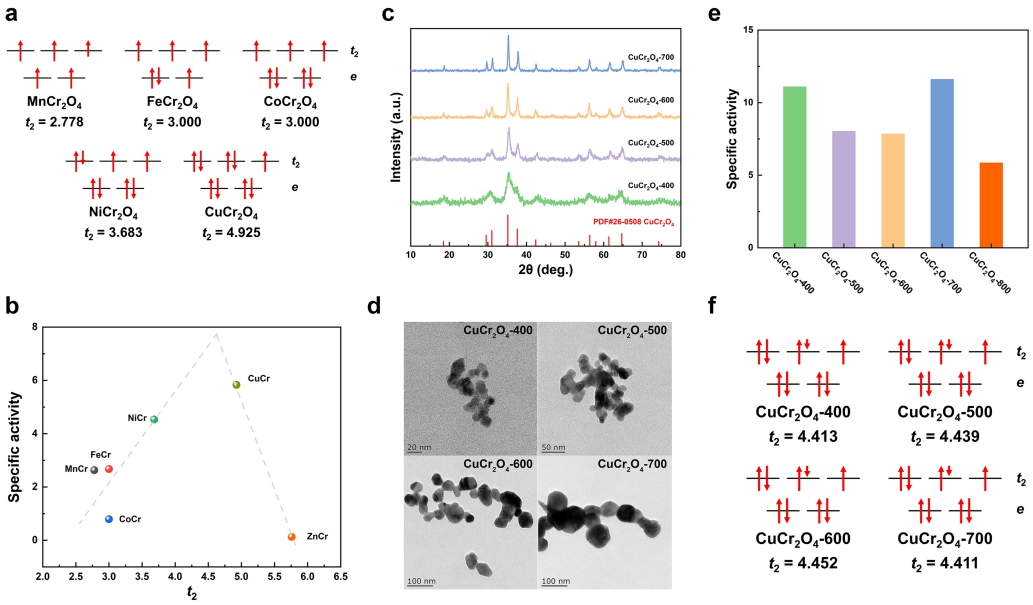

Figure 2. (a) Electron arrangements of d-orbital and t_2 occupancies of A site of ACr_2O_4 (A=Mn, Fe, Co, Ni, and Cu). (b) Specific activity as a function of t_2 occupancy of Cr-series spinel oxide nanozymes, here the names of spinel oxides were abbreviated. (c) XRD patterns of $CuCr_2O_4$-400, −500, −600, and −700. (d) TEM images of $CuCr_2O_4$-400, −500, −600, and −700. (e) Specific POD-like activities of $CuCr_2O_4$-400, −500, −600, −700 and −800. (f) Electron arrangements of d-orbital and t_2 occupancies of A site of $CuCr_2O_4$-400, −500, −600, and −700.

ing t_2 occupancy as the x-axis, revealing a potential non-monotonic correlation (volcanic curve) between t_2 occupancy and specific activity (Figure 2b). This volcanic relationship indicated the effectiveness of t_2 occupancy as a descriptor. As shown in Figure 2a-b, on the left side of the volcanic curve were $MnCr_2O_4$, $FeCr_2O_4$, $CoCr_2O_4$, and $NiCr_2O_4$. Their t_2 occupancies were 2.778, 3.000, 3.000, and 3.683, respectively, which were all less than 3.7. On the right side of the volcanic curve were $CuCr_2O_4$ and $ZnCr_2O_4$ with t_2 occupancies of 4.925 and 5.760, respectively. Both were more than 4.9. The above results revealed that the material occupying the apex of the volcanic curve should possess the highest activity, with t_2 occupancy between 3.7 and 4.9. Therefore, our next step was to adjust the t_2 occupancy towards the apex of the volcanic curve to obtain the material with the highest POD-like activity.

Further evaluating t_2 Occupancy as a Descriptor and Tuning It to Optimize and Obtain a Spinel Material with the Highest Activity

$CuCr_2O_4$ with relatively higher POD-like activity compared to other Cr-series oxides was selected as the research object to optimize the t_2 occupancy. Considering that the calcination temperature can affect the structural characteristics of spinel oxide catalysts,[17b,23] we tuned the calcination temperature to optimize the t_2 occupancy for further evaluating the correlation between t_2 occupancy and specific activity, aiming to obtain the material with the highest POD-like activity. Since the calcination temperature of $CuCr_2O_4$ investigated above was 800 °C ($CuCr_2O_4$-800), we also synthesized $CuCr_2O_4$ with calcination temperatures of 400, 500, 600, and 700 °C ($CuCr_2O_4$-400, −500, −600, and −700, respectively). The same methods were conducted to fully characterize these nanomaterials (Figures 2c-d, S7, S9, and S10, and Tables S1–S3). The TEM images (Figure 2d) revealed that all as-prepared $CuCr_2O_4$ samples were uniform nanoscale particles with no specific morphology, the different calcination temperatures resulted in different sizes of nanoparticles. The XRD patterns of the as-prepared $CuCr_2O_4$ samples (Figure 2c) displayed a set of identical peaks corresponding to $CuCr_2O_4$ standard card (red line, PDF#26–0508) and matched well with it, indicating a typical spinel structure. XPS spectra (Figure S7) of Cu 2p at around 954.7 eV and 934.6 eV corresponed to Cu^{2+} $2p_{1/2}$ and Cu^{2+} $2p_{3/2}$, Cr 2p at around 585.9 eV and 576.6 eV represented Cr^{3+} $2p_{1/2}$ and Cr^{3+} $2p_{3/2}$, though a slight peak shift was observed in different calcination temperatures. These results demonstrated the successful synthesis of $CuCr_2O_4$ with different calcination temperatures.

The same methods were used to determine the specific activities of $CuCr_2O_4$ with different calcination temperatures (Figures S8–S9). As shown in Figure 2e, the specific activity was indeed related to calcination temperature, increasing to nearly twofold for $CuCr_2O_4$-400 and $CuCr_2O_4$-700 compared to $CuCr_2O_4$-800. Similarly, the accurate electronic arrangements of $CuCr_2O_4$ with different calcination temperatures and the corresponding t_2 occupancies of A site were obtained (Figures 2f and S10, and Tables S2–S3).

The specific activities and t_2 occupancies of $CuCr_2O_4$ with calcination temperatures 400–700 °C were supplemented to the volcanic curve and matched well with it (Figure 3a). When t_2 occupancy reached 4.411, the spinel nanomaterial $CuCr_2O_4$-700 occupied the apex of the volcanic curve and exhibited the highest specific activity, which was consistent with our prediction. The above results and the excellent volcanic curve further demonstrated that t_2 occupancy was indeed an effective and predictive descriptor that can guide the design of nanozymes.

As shown in Figure 3a, $CuCr_2O_4$-400, −500, −600, and −700 possessed similar t_2 occupancies of around 4.4, locating at similar x-coordinates of the vertex of the volcanic curve. They all displayed better specific activities compared to other as-prepared Cr-series spinel oxide nanozymes. Therefore, it was imperative to identify a factor to interpret the differences in their specific activities despite similar t_2 occupancies. Considering that the different calcination temperatures can introduce varying degrees of defects, and the POD-like catalytic process generally occurs on the surface of the nanomaterials, we carried out the XPS measurements to investigate the surface properties of the as-prepared Cr-series spinel oxides. Since O_β from defective sites plays an important role in the catalytic process,[24] we fitted the XPS spectra of O 1s to differentiate between lattice oxygen (O_α) and surface oxygen (O_β) (Figures S11 and S12). We obtained the O_β content of the as-prepared samples, as shown in Table S5. Encouragingly, when we plotted O_β content on the x-axis against the specific activity of $CuCr_2O_4$ with different calcination temperatures on the y-axis, a strong linear relationship was observed (Figure 3b). Therefore, O_β content was introduced as a secondary descriptor to interpret the results of different specific activities of these materials while possessing similar t_2 occupancies. Similarly, $CoCr_2O_4$ had a significantly lower O_β content than $FeCr_2O_4$, resulting in the lower specific activity than $FeCr_2O_4$ though possessing the same t_2 occupancy.

Dual Descriptors Strategy Drove a 3D Volcanic Curve

The above results suggested that t_2 occupancy was indeed an effective and predictive descriptor. In addition, O_β content can also describe the specific activities when t_2 occupancies were the same. Therefore, the dual descriptors strategy was proposed (Figure 3c): t_2 occupancy was the primary descriptor that mainly affected the specific activity and can guide the design of nanozymes and even other catalysts, while O_β content was the secondary descriptor that can be used to further improve the catalytic performance of materials when t_2 occupancy was approximately the same.

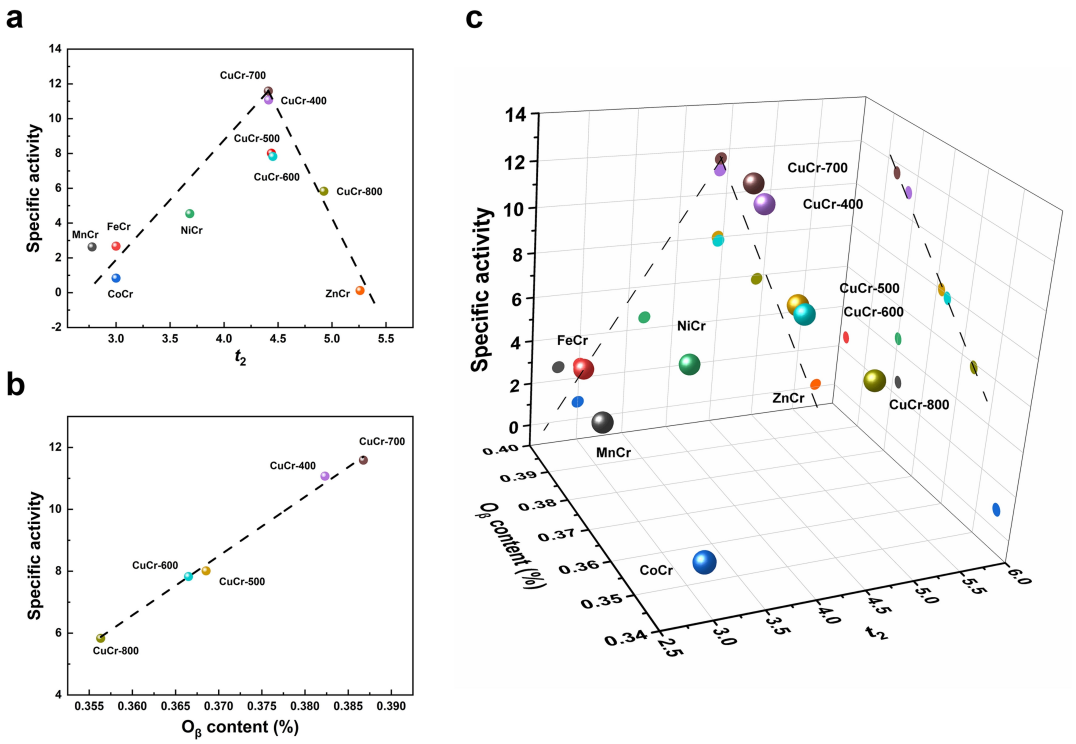

Figure 3. (a) Specific POD-like activity of the Cr-series spinel oxide nanozymes as a function of t_2 occupancy. (b) Specific POD-like activity of the $CuCr_2O_4$ with different calcination temperatures as a function of O_β content. (c) Specific POD-like activity of the Cr-series spinel oxide nanozymes as functions of both t_2 and O_β content. Here the names of spinel oxides were all abbreviated.

Dual Sites Regulating Strategy Beyond the Limits of Volcanic Curve for Higher Performance Optimization

The above results revealed that when Cu occupied the tetrahedral site with an AO_4 structure, spinel oxide nanozymes showed the highest specific activity. Previously, we revealed that when Co occupied the octahedral site with a BO_6 structure, the material $LiCo_2O_4$ exhibited the highest activity at that time.[5b] By combining these two works of research on tetrahedral site with an AO_4 structure (this work) and octahedral site with a BO_6 structure (previous work), we reported the dual sites optimizing strategy to simultaneously control both sites for the optimal elements. Specifically, when the A site was occupied by Cu and the B site was occupied by Co, the material $CuCo_2O_4$ was designed. We synthesized $CuCo_2O_4$ with a solvothermal method.[25] In addition, we synthesized Cu-doped $LiCo_2O_4$ (Cu–$LiCo_2O_4$) with a solvothermal method[25] and $LiCo_2O_4$ with a sol-gel method.[26] We compared these three materials with the as-prepared $CuCr_2O_4$ (Figure 4).

The TEM images (Figure 4a-c) revealed that all as-prepared samples were uniform nanoscale particles with no specific morphology features. The XRD patterns of as-prepared samples (Figure 4d) were well-matched with $CuCo_2O_4$ standard card (red line, PDF#37-0878), indicating a typical spinel structure. These results demonstrated the successful synthesis of $CuCo_2O_4$, Cu-$LiCo_2O_4$, and $LiCo_2O_4$. We used the same methods to investigate their specific activities (Figures S13 and S14). $CuCo_2O_4$ optimized by the dual sites optimization strategy with intrinsic POD-like activity showed the highest specific activity (Figures 4e and S15), achieving around 2-fold and 100-fold improvements in specific activity than $LiCo_2O_4$ and $CuCr_2O_4$-700, respectively. This result surmounted the vertexes of the two volcanic curves, indicating the capacity of breaking through the limits of volcanic curve.

For the optimized $CuCo_2O_4$ nanozyme, the catalytic activity under different pH was investigated (Figure S16). $CuCo_2O_4$ exhibited pH-dependent activity with significant activity in acidic environments. Afterward, the stability of $CuCo_2O_4$ was systematically investigated. Only a negligible decrease in the activity of $CuCo_2O_4$ was observed in the cycling experiments (Figure S17). It should be noted that the depletion of activity can be partially attributed to the loss of material during the centrifugal process and the effect of adsorption of the product (oxTMB) on the nanozyme surface. The XRD pattern of $CuCo_2O_4$ after reaction still matched well with the corresponding $CuCo_2O_4$ standard card (Figure S18). In addition, the XPS spectra of Co 2p of fresh and reacted $CuCo_2O_4$ were shown in Figure S19. The two peaks at 794.8 eV and 779.6 eV, assigned to Co $2p_{1/2}$ and Co $2p_{3/2}$, respectively, can be deconvoluted into the peaks of Co^{3+}, Co^{2+}, and satellites.[27] The ratios of fresh and reacted $CuCo_2O_4$ were 1.40 and 1.50, respectively, indicating no significant change of average metal valence after reaction. The above results confirmed the satisfactory stability of $CuCo_2O_4$. To demonstrate the importance and advantages of the predictively obtained materials, the comparison of K_m

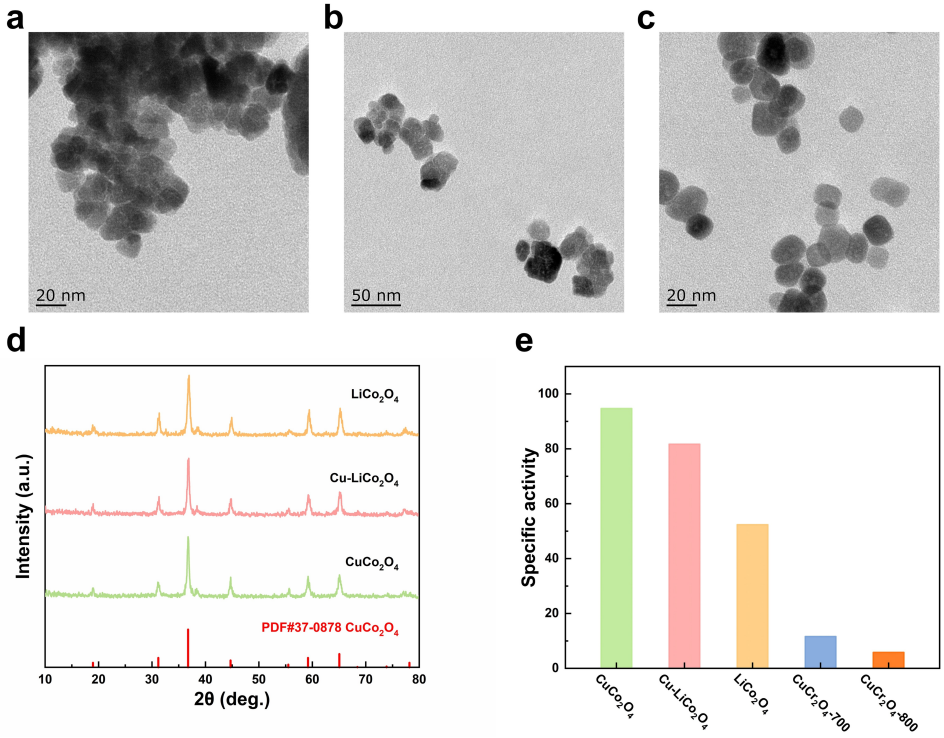

Figure 4. (a-c) TEM images of $CuCo_2O_4$, Cu-$LiCo_2O_4$, and $LiCo_2O_4$ (d) XRD patterns of $CuCo_2O_4$, Cu-$LiCo_2O_4$, and $LiCo_2O_4$. (e) Comparison of the specific POD-like activities of $CuCo_2O_4$, Cu-$LiCo_2O_4$, $LiCo_2O_4$, $CuCr_2O_4$-700, and $CuCr_2O_4$-800.

and V_{max} in POD-like activity of $CuCo_2O_4$ with typical metal oxide nanozymes and HRP was listed (Table S6).

DFT Calculations

DFT calculations were performed to investigate the potential microscopic catalytic mechanism and structure–activity relationship of the spinel oxide nanozymes (referring to the Experimental Section for details). The proposed mechanism of the spinel oxide nanozymes as POD mimics followed two steps,[28] as shown in Figure 5a: i) the adsorption of H_2O_2 molecules on the surface of spinel oxides and subsequent decomposition to form the adsorbed dihydroxyl intermediates (2OH*); ii) two successive reduction processes of the adsorbed hydroxyl groups (OH*) by TMB, reacting through the protonation-coupled transfer process of H atom from the TMB substrates to each adsorbed hydroxyl and generating H_2O.

The structures and energy values involved in the POD-like catalytic process are shown in Figures 5 and S20. According to the energy profiles shown in Figure 5b, the adsorption and decomposition step of H_2O_2 into 2OH* had a large exothermicity with energy ranging from −2.00 eV to −5.71 eV. Especially for ACr_2O_4 due to their stronger reducibility, H_2O_2 could directly decompose into 2OH* on the surface without an adsorption form (H_2O_2*). Thus, step i) was not the rate-determining step (RDS). Removing one hydroxyl group from the surface of dihydroxyl absorbed was easier than from the surface of one hydroxyl absorbed, as the structure with two hydroxyls absorbed was more oxidized than that with one hydroxyl absorbed.[28] Consequently, step iib) rather than step iia) was the RDS of these spinel oxide nanozymes. The RDS had an energy range from −0.86 eV to 1.30 eV. Based on the Brønsted-Evans-Polanyi (BEP) relationship, the activation energy is proportional to the reaction energy for a chemical reaction. Consequently, the activation energy followed the order: −0.86 eV ($CuCo_2O_4$) < −0.66 eV ($LiCo_2O_4$) <0.82 eV ($CuCr_2O_4$) <0.85 eV ($NiCr_2O_4$) <0.91 eV ($MnCr_2O_4$) <1.31 eV ($ZnCr_2O_4$). Therefore, the activities followed the order: $CuCo_2O_4 > LiCo_2O_4 > CuCr_2O_4 > NiCr_2O_4 > MnCr_2O_4 > ZnCr_2O_4$, which was consistent with experimental results.

Alternatively, our previous report indicated that the adsorption energy of OH ($E_{ads,\ OH}$) is a good descriptor to explain and predict the POD-like activities.[28] As shown in Table S9, the calculated $E_{ads,\ OH}$ of $ZnCr_2O_4$, $MnCr_2O_4$, $NiCr_2O_4$, $CuCr_2O_4$, and $LiCo_2O_4$ were ascending sequentially, and all of them were less than the maximum activity value (−2.6 eV) of POD-like reaction. Accordingly, their POD-like activities were also ascending sequentially. The $E_{ads,\ OH}$ of $CuCo_2O_4$ and $LiCo_2O_4$ were close to −2.6 eV, confirming the extremely high POD-like activities of $CuCo_2O_4$ and $LiCo_2O_4$ compared with other ACr_2O_4. Furthermore, for $CuCr_2O_4$ with varying O_β content due to different calcination temperatures, the higher O_β content induced the decrease of reducibility on the materials' surface, and consequently resulted in the increase of $E_{ads,\ OH}$

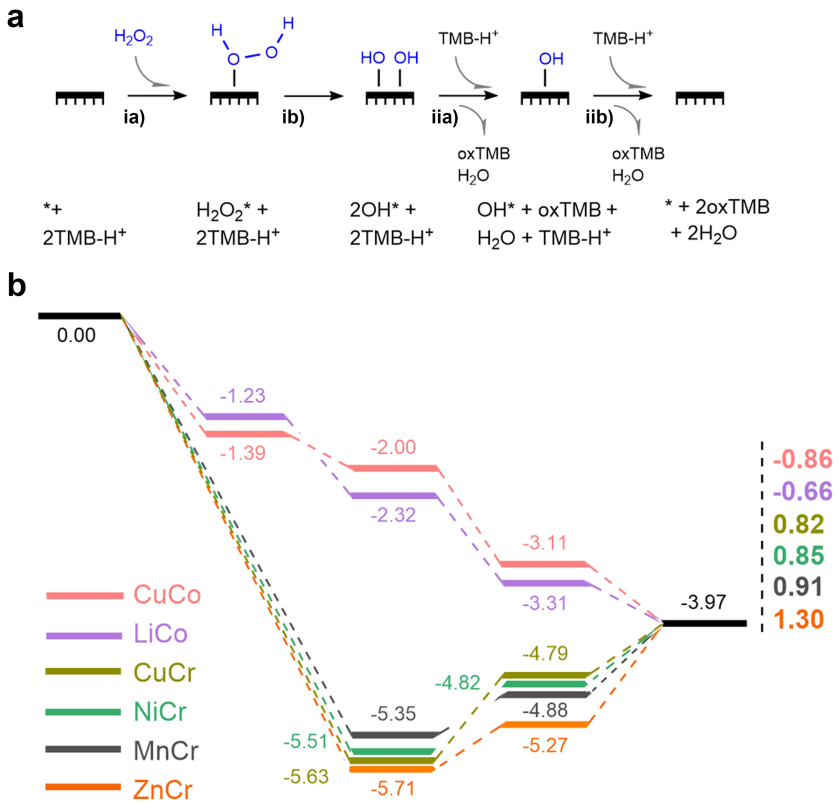

Figure 5. (a) Proposed mechanism of spinel oxide nanozymes for POD-like catalytic processes. The substrates and intermediates participating in every process were correspondingly listed below, where * denoted the adsorbed state. (b) Relative energies of corresponding intermediates participating in the POD-like catalytic processes of ACr_2O_4 (A=Mn, Ni, Cu, and Zn), $LiCo_2O_4$ and $CuCo_2O_4$. The units were eV. The names of spinel oxides were abbreviated.

to a more favorable range,[29] leading to the higher specific activity.

Conclusion

Through the rational design of spinel oxides, experimental explorations, and DFT calculations, we first reported and identified the effectiveness and predictive capacity of t_2 occupancy as a descriptor of spinel oxide nanozymes for the tetrahedral site. The POD-like activity of Cr-series spinel oxide nanozymes was demonstrated to possess a non-monotonic volcanic curve relationship with t_2 occupancy. After tuning t_2 occupancy, the optimized materials with t_2 occupancy of around 4.4 matched well with the volcanic curve and reached its vertex. Moreover, we observed that the O_β content possessed an excellent linear relationship with specific activity, leading us to introduce it as a secondary descriptor while t_2 occupancy was the primary descriptor. The dual descriptors strategy drove a 3D volcanic curve, converging at a vertex. Subsequently, to break through the limitations of volcanic curves, we proposed the dual sites regulating strategy for optimizing A and B sites as Cu and Co, respectively. Encouragingly, $CuCo_2O_4$ with the highest POD-like activity and excellent stability was obtained. DFT calculations provided a thorough understanding of microscopic catalytic mechanism and structure-activity relationship of the POD-like catalytic process. t_2 occupancy was identified as a direct descriptor for the first time, demonstrating its effectiveness and predictive power. We believe it will greatly promote research on the activity, design, and application of nanozymes as well as other catalytic fields.

Acknowledgements

This work was supported by National Key R&D Program of China (2021YFF1200700 and 2019YFA0709200), Jiangsu Provincial Key R&D Program-Social Development (BE2022836), National Natural Science Foundation of China (22374071 and 11874199), PAPD Program, State Key Laboratory of Analytical Chemistry for Life Science (5431ZZXM2306), and Fundamental Research Funds for the Central Universities.

Conflict of Interest

The authors declare no conflict of interest.

Data Availability Statement

The data that support the findings of this study are available from the corresponding author upon reasonable request.

Keywords: t_2 occupancy · activity descriptor · spinel oxides · nanozymes · peroxidase mimics

[1] H. Wei, E. Wang, *Chem. Soc. Rev.* **2013**, *42*, 6060–6093.

[2] a) M. Liang, X. Yan, *Acc. Chem. Res.* **2019**, *52*, 2190–2200; b) Y. Huang, J. Ren, X. Qu, *Chem. Rev.* **2019**, *119*, 4357–4412; c) R. Zhang, X. Yan, K. Fan, *Acc. Mater. Res.* **2021**, *2*, 534–547; d) Y. Zhang, G. Wei, W. Liu, T. Li, Y. Wang, M. Zhou, Y. Liu, X. Wang, H. Wei, *Nat. Rev. Methods Primers* **2024**, *4*, 36; e) R. Zhang, B. Jiang, K. Fan, L. Gao, X. Yan, *Nat. Rev. Bioeng.* **2024**, *2*, 849–868; f) R. Zeng, Q. Gao, L. Xiao, W. Wang, Y. Gu, H. Huang, Y. Tan, D. Tang, S. Guo, *J. Am. Chem. Soc.* **2024**, *146*, 10023–10031; g) J. Xu, M. Wu, J. Yang, D. Zhao, D. He, Y. Liu, X. Yan, Y. Liu, D. Pu, Q. Tan, L. Zhang, J. Zhang, *Nat. Nanotechnol.* **2024**, *19*, 1544–1557; h) J. Lee, X. A. Le, H. Chun, T. H. Vu, D. Choi, B. Han, M. I. Kim, J. Lee, *Biosens. Bioelectron.* **2024**, *246*, 115882.

[3] L. Gao, J. Zhuang, L. Nie, J. Zhang, Y. Zhang, N. Gu, T. Wang, J. Feng, D. Yang, S. Perrett, X. Yan, *Nat. Nanotechnol.* **2007**, *2*, 577–583.

[4] a) D. Xu, L. Wu, H. Yao, L. Zhao, *Small* **2022**, *18*, 2203400; b) J. Sheng, Y. Wu, H. Ding, K. Feng, Y. Shen, Y. Zhang, N. Gu, *Adv. Mater.* **2024**, *36*, 2211210.

[5] a) X. Wang, X. J. Gao, L. Qin, C. Wang, L. Song, Y.-N. Zhou, G. Zhu, W. Cao, S. Lin, L. Zhou, K. Wang, H. Zhang, Z. Jin, P. Wang, X. Gao, H. Wei, *Nat. Commun.* **2019**, *10*, 704; b) Q. Wang, C. Li, X. Wang, J. Pu, S. Zhang, L. Liang, L. Chen, R. Liu, W. Zuo, H. Zhang, Y. Tao, X. Gao, H. Wei, *Nano Lett.* **2022**, *22*, 10003–10009; c) Z. Chen, Y. Yu, Y. Gao, Z. Zhu, *ACS Nano* **2023**, *17*, 13062–13080; d) Y. Jiang, Z. Chen, N. Sui, Z. Zhu, *J. Am. Chem. Soc.* **2024**, *146*, 7565–7574.

[6] A. J. Medford, A. Vojvodic, J. S. Hummelshøj, J. Voss, F. Abild-Pedersen, F. Studt, T. Bligaard, A. Nilsson, J. K. Nørskov, *J. Catal.* **2015**, *328*, 36–42.

[7] a) F. H. B. Lima, J. Zhang, M. H. Shao, K. Sasaki, M. B. Vukmirovic, E. A. Ticianelli, R. R. Adzic, *J. Phys. Chem. C* **2007**, *111*, 404–410; b) H. B. Tao, L. Fang, J. Chen, H. B. Yang, J. Gao, J. Miao, S. Chen, B. Liu, *J. Am. Chem. Soc.* **2016**, *138*, 9978–9985; c) R. Jacobs, J. Hwang, Y. Shao-Horn, D. Morgan, *Chem. Mater.* **2019**, *31*, 785–797; d) C. Wei, Z. Feng, G. G. Scherer, J. Barber, Y. Shao-Horn, Z. J. Xu, *Adv. Mater.* **2017**, *29*, 1606800; e) J. Suntivich, K. J. May, H. A. Gasteiger, J. B. Goodenough, Y. Shao-Horn, *Science* **2011**, *334*, 1383–1385; f) A. Vojvodic, J. K. Nørskov, *Science* **2011**, *334*, 1355–1356; g) J. Suntivich, H. A. Gasteiger, N. Yabuuchi, H. Nakanishi, J. B. Goodenough, Y. Shao-Horn, *Nat. Chem.* **2011**, *3*, 546–550.

[8] H.-Y. Wang, S.-F. Hung, H.-Y. Chen, T.-S. Chan, H. M. Chen, B. Liu, *J. Am. Chem. Soc.* **2016**, *138*, 36–39.

[9] a) Q. Zhao, Z. Yan, C. Chen, J. Chen, *Chem. Rev.* **2017**, *117*, 10121–10211; b) C. Shan, Y. Wang, J. Li, Q. Zhao, R. Han, C. Liu, Q. Liu, *Environ. Sci. Technol.* **2023**, *57*, 9495–9514.

[10] M. Feng, X. Zhang, Y. Huang, *Talanta* **2024**, *271*, 125714.

[11] T. Phan-Xuan, S. Schweidler, S. Hirte, M. Schüller, L. Lin, A. Khandelwal, K. Wang, J. Schützke, M. Reischl, C. Kübel, H. Hahn, G. Bello, J. Kirchmair, J. Aghassi-Hagmann, T. Brezesinski, B. Breitung, L. A. Dailey, *ACS Nano* **2024**, *18*, 19024–19037.

[12] N. Song, Y. Yu, Y. Zhang, Z. Wang, Z. Guo, J. Zhang, C. Zhang, M. Liang, *Adv. Mater.* **2024**, *36*, 2210455.

[13] L. Fan, X. Xu, C. Zhu, J. Han, L. Gao, J. Xi, R. Guo, *ACS Appl. Mater. Interfaces* **2018**, *10*, 4502–4511.

[14] J. Sun, H. Xue, Y. Zhang, X.-L. Zhang, N. Guo, T. Song, H. Dong, Y. Kong, J. Zhang, Q. Wang, *Nano Lett.* **2022**, *22*, 3503–3511.

[15] a) M. Gul, *Mater. Res. Bull.* **2016**, *76*, 431–435; b) M. Ptak, M. Maczka, A. Gągor, A. Pikul, L. Macalik, J. Hanuza, *J. Solid State Chem.* **2013**, *201*, 270–279.

[16] T. Ramachandran, F. Hamed, *Mater. Res. Bull.* **2017**, *95*, 104–114.

[17] a) M. Mączka, M. Ptak, M. Kurnatowska, J. Hanuza, *Mater. Chem. Phys.* **2013**, *138*, 682–688; b) W. Yuan, X. Liu, L. Li, *Appl. Surf. Sci.* **2014**, *319*, 350–357.

[18] K. Manjunatha, V. Jagadeesha Angadi, R. A. P. Ribeiro, E. Longo, M. C. Oliveira, M. R. D. Bomio, S. R. de Lázaro, S. Matteppanavar, S. Rayaprol, P. D. Babu, M. Pasha, *J. Magn. Magn. Mater.* **2020**, *502*, 166595.

[19] a) M. C. Biesinger, B. P. Payne, A. P. Grosvenor, L. W. M. Lau, A. R. Gerson, R. S. C. Smart, *Appl. Surf. Sci.* **2011**, *257*, 2717–2730; b) B. Grzybowska-Świerkosz, M. Ruszel, R. Grabowski, L. Kępiński, M. A. Małecka, J. Sobczak, *React. Kinet. Mech. Cat.* **2012**, *105*, 69–78.

[20] K. Manjunatha, H.-H. Chiu, M.-K. Ho, A. Bajorek, S. Y. Wu, N. Roy, S. Wang, S. O. Manjunatha, M. Ubaidullah, S. F. Shaikh, C. Prakash, A. Kumar, S. W. Joo, V. J. Angadi, M. Atif, *J. Electron. Mater.* **2025**, *54*, 675–685.

[21] a) S. S. Acharyya, S. Ghosh, R. Tiwari, C. Pendem, T. Sasaki, R. Bal, *ACS Catal.* **2015**, *5*, 2850–2858; b) S. S. Acharyya, S. Ghosh, R. Bal, *ACS Sustainable Chem. Eng.* **2014**, *2*, 584–589.

[22] Y. Li, S. Feng, Q. Lv, X. Kan, X. Liu, *J. Alloys Compd.* **2021**, *877*, 160224.

[23] S. Mobini, F. Meshkani, M. Rezaei, *J. Environ. Chem. Eng.* **2017**, *5*, 4906–4916.

[24] W. Guo, M. Zhang, Z. Lou, M. Zhou, P. Wang, H. Wei, *ChemCatChem* **2019**, *11*, 737–743.

[25] Y. Feng, J. Liu, D. Wu, Z. Zhou, Y. Deng, T. Zhang, K. Shih, *Chem. Eng. J.* **2015**, *280*, 514–524.

[26] Y. Zhou, S. Sun, J. Song, S. Xi, B. Chen, Y. Du, A. C. Fisher, F. Cheng, X. Wang, H. Zhang, Z. J. Xu, *Adv. Mater.* **2018**, *30*, 1802912.

[27] a) M. Li, Y. Dai, Z. Liu, S. Liang, Y. Han, L. Fan, Z. Li, B. Dong, Y. Guo, *Sens. Actuators, B* **2025**, *425*, 136980; b) S. Han, X. Chen, Y. Fan, Y. Zhang, Z. Yang, X. Kong, Z. Liu, Q. Liu, X. Zhang, *New J. Chem.* **2021**, *45*, 2030–2037.

[28] X. Shen, Z. Wang, X. Gao, Y. Zhao, *ACS Catal.* **2020**, *10*, 12657–12665.

[29] Z. Wang, X. Shen, X. Gao, Y. Zhao, *Nanoscale* **2019**, *11*, 13289–13299.

Manuscript received: November 9, 2024
Accepted manuscript online: January 17, 2025
Version of record online: January 28, 2025